Article

Not peer-reviewed version

Facile Microwave Production and Photocatalytic Activity of Bismuth Vanadate Nanoparticles over the Acid Orange 7

Nataša Tot *, Bojana Vasiljević, Slađana Davidović, Anđela Pustak, Ivan Marić, Jovana Prekodravac Filipović, Dragana Marinković *

Posted Date: 6 October 2025

doi: 10.20944/preprints202510.0388.v1

Keywords: Bismuth vanadate ($BiVO_4$); Microwave-assisted synthesis; Energy band gap; Visible-light photocatalysis; Acid Orange 7; Antibacterial properties; Wastewater treatment

 doi:10.20944/preprints202510.0388.v1

Article

Facile Microwave Production and Photocatalytic Activity of Bismuth Vanadate Nanoparticles over the Acid Orange 7

Nataša Tot [1,*], Bojana Vasiljević [1], Slađana Davidović [2], Anđela Pustak [3], Ivan Marić [3], Jovana Prekodravac Filipović [1] and Dragana Marinković [1,*]

[1] Vinča Institute of Nuclear Sciences, National Institute of the Republic of Serbia, University of Belgrade, P. O. Box 522, 11001 Belgrade, Serbia

[2] Faculty of Technology and Metallurgy, University of Belgrade, Department of Biochemical Engineering and Biotechnology, Karnegijeva 4, 11000, Belgrade, Serbia

[3] Radiation Chemistry and Dosimetry Laboratory, Ruđer Bošković Institute, Bijenička cesta 54, 10 000, Zagreb, Croatia

* Correspondence: natasa.tot@vin.bg.ac.rs (N.T); draganaj@vin.bg.ac.rs (D.M)

Abstract

This work presents the synthesis, characterization, and multifunctional properties of bismuth vanadate ($BiVO_4$) nanoparticles prepared by a rapid and eco-friendly microwave-assisted method. X-ray diffraction (XRD) confirmed the formation of monoclinic scheelite-type $BiVO_4$ with an average crystallite size of ~19 nm. Transmission electron microscopy (TEM) revealed nearly uniform nanoscale morphology, while Fourier-transform infrared spectroscopy (FTIR) verified the presence of characteristic Bi–O and V–O vibrational modes. Nitrogen adsorption–desorption analysis (BET) indicated a specific surface area of 7.5 m^2/g, consistent with a non-porous or weakly porous material. UV–Vis diffuse reflectance spectroscopy (DRS) determined a band gap of 2.55 eV, confirming visible-light activity. Photocatalytic performance was evaluated through the degradation of Acid Orange 7 (AO7) under visible-light irradiation. Effects of catalyst dosage and the initial concentration of pollutant Acid Orange 7 on photocatalytic degradation efficiency, were explained in details. Catalyst loading and initial dye concentration strongly influenced efficiency, achieving up to 77% removal within 120 minutes and well fitting to pseudo-first-order kinetics. In addition, the $BiVO_4$ nanoparticles exhibited notable antibacterial activity against *Escherichia coli*, attributed to synergistic effects of reactive oxygen species generation and direct surface interactions with bacterial membranes. These findings demonstrate that microwave-synthesized $BiVO_4$ is a multifunctional material with strong potential for integrated wastewater purification and disinfection applications.

Keywords: Bismuth vanadate ($BiVO_4$); Microwave-assisted synthesis; Energy band gap; Visible-light photocatalysis; Acid Orange 7; Antibacterial properties; Wastewater treatment

1. Introduction

Water is a fundamental natural resource, indispensable for sustaining life, ensuring human well-being, and maintaining ecosystem functionality. However, rising living standards are often accompanied by increased industrial production and consumption, which lead to excessive pollution of water, air, and soil [1]. The presence of pollutants such as pesticides, heavy metals, and pharmaceuticals in the environment can cause severe ecological and public health risks [2].

Among various contaminants in aquatic ecosystems, organic dyes represent a particularly concerning group due to their extensive use in industries such as textiles, leather, paper, food processing, and cosmetics [3,4]. Within this group, azo dyes are the most widely used, accounting for more than 60% of all synthetic dyes produced worldwide [5]. They are characterized by one or more

 doi:10.20944/preprints202510.0388.v1

azo bonds, which provide high chemical stability, strong color intensity, and remarkable resistance to light, temperature, and microbial degradation [5,6]. While these properties are desirable in industrial applications, they also make azo dyes extremely persistent in the environment. Moreover, their degradation products, including aromatic amines, are often toxic, mutagenic, or carcinogenic to humans and aquatic life [7]. A well-known representative of this group is AO7, an anionic azo dye widely used in textile dyeing and paper printing. Its complex aromatic structure makes AO7 highly resistant to conventional wastewater treatment methods, which poses a major environmental challenge [8].

Conventional water purification approaches, including coagulation, activated carbon adsorption, reverse osmosis, ultrafiltration, and biological treatments, are frequently insufficient for the effective elimination of these pollutants [9]. As a result, advanced oxidation processes (AOPs) have attracted considerable attention for the degradation of azo dyes, particularly AO7 [8,10]. These processes generate reactive oxygen species capable of mineralizing pollutants into non-toxic end products such as CO_2, water, and inorganic ions [11]. Within this context, heterogeneous photocatalytic processes have achieved significant progress, distinguished by their environmental compatibility and demonstrated efficiency in wastewater treatment and air purification [12,13].

The most widely studied photocatalyst is titanium dioxide (TiO_2), valued for its stability and low toxicity. However, its relatively wide band gap (3.0–3.2 eV for rutile and anatase) restricts its activity to UV irradiation, which accounts for only about 5% of sunlight [14,15]. Accordingly, recent studies have increasingly focused on visible-light-responsive photocatalysts, which are capable of harvesting a larger fraction of solar energy [16]. Among these, bismuth vanadate ($BiVO_4$) has emerged as a particularly promising candidate due to its relatively narrow band gap (~2.4 eV), high photostability, chemical inertness, non-toxicity, and facile synthesis methods [17–19]. Its electronic structure, involving O 2p and Bi 6s hybrid orbitals, facilitates visible-light absorption more efficiently than TiO_2, whose valence band consists only of O 2p orbitals [20]. The monoclinic scheelite phase of $BiVO_4$ is recognized for superior photocatalytic activity compared to tetragonal forms, mainly due to its narrower band gap and favorable charge transport properties. This has been repeatedly demonstrated in azo dye degradation under visible-light irradiation [21,22].

Further modifications enhance $BiVO_4$ performance by improving light absorption and reducing charge recombination. Europium doping, for instance, extended the lifetime of photoexcited electrons and enabled 90% degradation of Methyl Orange within 180 minutes under visible light [23]. Heterojunction formation has also proven highly effective. $BiVO_4/TiO_2$ composite achieved complete degradation of Acid Blue 113 in just 20 minutes [24], while AgBr-decorated $BiVO_4$ reached ~93% removal of AO7 in 80 minutes under visible-light irradiation [25].

In addition to its well-established photocatalytic performance, $BiVO_4$ has also been increasingly recognized as an effective antimicrobial agent against both Gram-positive and Gram-negative bacteria, primarily through mechanisms involving the generation of reactive oxygen species (ROS) and the resulting oxidative stress that compromises cellular membranes and essential biomolecules [17,26]. Microwave-synthesized $BiVO_4$ nanoparticles have been shown to significantly inhibit the growth of *Escherichia coli* and *Staphylococcus aureus*, thereby confirming their combined photocatalytic and antibacterial functionality [26–28]. Furthermore, ultra-small tetragonal zircon-type $BiVO_4$ nanoparticles (2–8 nm) obtained via an ethylene glycol-assisted method were reported to induce severe bacterial cell wall damage, which was attributed to the synergistic effect of ROS formation and electrostatic interactions between positively charged Bi^{3+} surface sites and negatively charged bacterial membranes [29,30] . Collectively, these results underscore the potential of $BiVO_4$ as a multifunctional material capable of simultaneously enabling pollutant degradation and efficient microbial inactivation, which is of particular importance for integrated water treatment and disinfection applications.

Based on these advantages, the present study aims to synthesize, characterize, and evaluate the photocatalytic and antibacterial properties of $BiVO_4$ nanoparticles. The material was obtained using a rapid, cost-effective, and eco-friendly microwave-assisted method, which ensures uniform heating,

 doi:10.20944/preprints202510.0388.v1

shorter reaction times, and improved energy efficiency. The obtained $BiVO_4$ nanoparticles were characterized by XRD to determine the crystal structure and crystallite size, TEM to examine morphology and particle size, BET analysis to assess porosity and specific surface area, and FTIR to identify functional groups. Photocatalytic activity was evaluated through the degradation of AO7 under visible-light irradiation at the natural pH of the solution, with emphasis on the effects of catalyst dosage and initial dye concentration. Furthermore, the antibacterial properties of $BiVO_4$ nanoparticles were investigated against representative bacterial strain, highlighting their potential as a dual-action material for integrated wastewater remediation and disinfection applications.

2. Materials and Methods

2.1. Materials

All reagents were of analytical grade and used without further purification. Table 1 summarizes the main chemicals applied in the synthesis and photocatalytic experiments.

Table 1. The main chemical reagents used in the experiments.

Reagent Name	Chemical formula	Purity	CAS No.
Bismuth nitrate pentahydrate	$Bi(NO_3)_3 \times 5H_2O$	≥99% (AR)	10035-06-0
Ammonium metavanadate	NH_4VO_3	99 %	7803-55-6
Nitric acid	HNO_3	≥99% (AR)	7697-37-2
Acid Orange 7(AO7)	$C_{16}H_{11}N_2NaO_4S$	95% (dye grade)	633-96-5

2.2. Synthesis of $BiVO_4$

$BiVO_4$ was synthesized via a microwave-assisted process. An aqueous solution of $Bi(NO_3)_3{\cdot}5H_2O$ (5 mL, 0.05 M) was combined with NH_4VO_3 (5.5 mL, 0.05 M) in a G30 process vial equipped with a magnetic stir bar. The mixture was magnetically stirred for 5 minutes to achieve homogeneity and subsequently sealed with a septum and standard reactor cap. The reaction was carried out in a closed-vessel microwave reactor under temperature-control mode at 170 °C for 10 min. After cooling to room temperature, the resulting suspension was transferred to centrifuge tubes and subjected to centrifugation at 12,000 rpm for 20 minutes. The obtained precipitate was washed three times with deionized water and ethanol to remove residual ions and then dried in a vacuum oven at 70 °C for 180 minutes. A light-yellow powder of monoclinic $BiVO_4$ was obtained with a yield of approximately 98%.

2.3. Characterization

XRD measurements were carried out using a BRUKER AXS GMBH, A24A10 diffractometer equipped with Cu Kα radiation (λ = 0.15406 nm), operated at 40 kV and 30 mA. Diffraction data were recorded at room temperature over a 2θ range of 10–70°, with a scanning speed of 3°/min and a 0.5 mm divergent slit. The crystallite size was determined from the most intense diffraction peak by applying the Scherrer equation (Eq. (1)):

$$D = \frac{k\lambda}{\beta\cos\theta} \quad (1)$$

where D represents the crystallite size, k is the shape factor, λ the X-ray wavelength, β the full width at half maximum (FWHM), and θ the Bragg angle.

TEM measurements were performed using a FEI Tecnai F20 at 200 kV electron acceleration voltage after drop- casting of sample material on lacey carbon TEM grids.

The textural properties of the material were examined by nitrogen adsorption–desorption isotherms recorded at 77 K using a Quantachrome Autosorb iQ3 analyzer. Prior to measurement, the

 doi:10.20944/preprints202510.0388.v1

sample was degassed under vacuum by stepwise heating at 90 °C for 1 h and subsequently at 200 °C, until the pressure rise rate was below 50 millitorr min^{-1}, indicating complete removal of adsorbed gases and moisture. The specific surface area was calculated by the Brunauer–Emmett–Teller (BET) method in the relative pressure range of 0.05–0.30, and pore characteristics were derived from the shape of the isotherm.

FTIR spectroscopy was carried out on a Thermo Scientific Nicolet iS50 spectrometer equipped with a built-in all-reflective ATR diamond accessory. Spectra were recorded in the range of 400–4000 cm^{-1} with a spectral resolution of 4 cm^{-1} at room temperature.

The optical properties were evaluated by UV–Vis DRS using a Shimadzu 1800 spectrophotometer equipped with an integrating sphere in the wavelength range of 300–800 nm. The reflectance data were converted into absorbance using the Kubelka–Munk function (Eq. (2)):

$$\mathrm{F(R)} = \frac{(1-R)^2}{2\mathrm{R}} \tag{2}$$

where R is the observed reflectance.

The optical band gap (Eg) was then estimated according to the Tauc relation (Eq. (3)):

$$\mathrm{F((FKM(R)} \times h\nu)^{1/\mathrm{n}} = \mathrm{A\ (hv - Eg)} \tag{3}$$

where $F_{KM}(R)$ is the Kubelka–Munk function; R is the observed reflectance in the UV-Vis spectrum; *hν* is the photon energy; A is a proportionality constant, and n characterizes the electronic transition type. Since $BiVO_4$ is a direct-allowed semiconductor, the value n=1/2 was applied in the Tauc's relation.

2.4. Photocatalytic Activity Evaluation

The photocatalytic activity of $BiVO_4$ was evaluated through the degradation of AO7 aqueous solution under visible light irradiation. A 500 W xenon lamp was used as the illumination source, positioned at a distance of 30 cm from the surface of the reaction mixture.

In a typical experiment, a given mass of $BiVO_4$ (10, 15, or 20 mg, depending on the run) was dispersed in 50 mL of AO7 solution with an initial concentration of 15, 20, or 25 ppm. The suspension was first treated in an ultrasonic bath for 15 min and subsequently stirred in the dark for 60 min to ensure adsorption–desorption equilibrium between AO7 and $BiVO_4$.

During irradiation, aliquots of 1.5 mL were withdrawn at predetermined time intervals (up to 120 min), centrifuged at 12,000 rpm for 20 min to remove the catalyst, and the supernatant was analyzed by UV–Vis spectroscopy. The concentration of AO7 was monitored at its absorption maximum (λmax ≈ 484 nm).

The degradation efficiency (D) was calculated using Equation (4):

$$D(\%) = \frac{Co - Ct}{Co} \times 100 \tag{4}$$

where C_0 is the initial concentration of AO7 and C_t the concentration after irradiation time.

The photocatalytic degradation kinetics were analyzed according to the Langmuir–Hinshelwood pseudo-first-order model (Eq. (5)):

$$-ln\left(\frac{Ct}{Co}\right) = Kt \times t \tag{5}$$

where Kt is the apparent pseudo-first-order rate constant.

2.5. Antibacterial Properties

Antimicrobial activity of the $BiVO_4$ nanoparticles was examined against the Gram-negative bacterium Escherichia coli ATCC 25922. An overnight culture of E. coli was prepared in tryptic soy

 doi:10.20944/preprints202510.0388.v1

broth (Torlak, Serbia) supplemented with 0.6% yeast extract (Torlak, Serbia). The culture was centrifuged, washed twice with sterile physiological saline (0.9% NaCl), and resuspended to a final concentration of approximately 10^7 CFU/mL. Afterwards, 100 µL of the bacterial suspension was added to 9.9 mL of a $BiVO_4$ nanoparticle suspension (1 mg/mL), which had been previously irradiated with UV light for 30 minutes to enhance photocatalytic activity. The sample was incubated at 37 °C with shaking at 120 rpm for 4 hours, in parallel with control (E. coli without $BiVO_4$). Following incubation, serial decimal dilutions were prepared and plated on sterile tryptic soy agar (TSA) plates. The plates were incubated for 24 hours at 37 °C, after which colony-forming units (CFU) were counted. Percent of bacterial growth inhibition was calculated as follows (Eq. (6)):

$$R(\%) = \frac{Co - C}{Co} \times 100 \quad (6)$$

where C_0 is the number of CFU from the control sample and C is the number of CFU from the treated sample.

The experiment was performed in triplicate and statistical analysis of the results was performed using OriginPro (OriginLab Corporation, Northampton, MA, USA). One-way analysis of variance (ANOVA), followed by Tukey's test, was used to determine statistical significance. A p-value of $p<0.05$ was considered statistically significant.

3. Results and Discussion

3.1. Structural and Morphological Properties of the Microwave-Synthesized $BiVO_4$

Figure 1 illustrates the structural and morphological characterization of the synthesized $BiVO_4$ powder. The XRD pattern (Figure 1a) reveals diffraction peaks that are in excellent agreement with the reference standard (JCPDS card No. 01-074-4894), confirming the formation of a single-phase monoclinic scheelite-type structure (clinobisvanite, space group *I2/b*). The main diffraction peaks observed at approximately 18.9°, 28.9°, 30.5°, 35.2°, and 39.7° were indexed to the (011), (112), (004), (020), and (211) planes of monoclinic $BiVO_4$, respectively, confirming that the microwave-assisted synthesis yielded a highly crystalline and phase-pure material. The average crystallite size, estimated from the most intense reflection at $2\theta \approx 28.9°$ using the Scherrer approach, was found to be around 19 nm.

Complementary TEM observations (Figure 1b) provide further insight into the microscopic morphology of the $BiVO_4$ nanoparticles. The TEM micrograph reveals well-defined nanosized particles with relatively uniform distribution with size approximately of 20 nm, which is in full agreement with the crystallite size calculated from XRD (~19 nm). Most of the nanoparticles exhibit near-spherical to slightly irregular shapes, which is characteristic of microwave-assisted synthesis due to rapid nucleation and growth [17,20]. The image also indicates that the majority of the particles are discrete, although some degree of agglomeration can be observed, which is commonly reported for $BiVO_4$ nanoparticles owing to their high surface energy [21,26].

 doi:10.20944/preprints202510.0388.v1

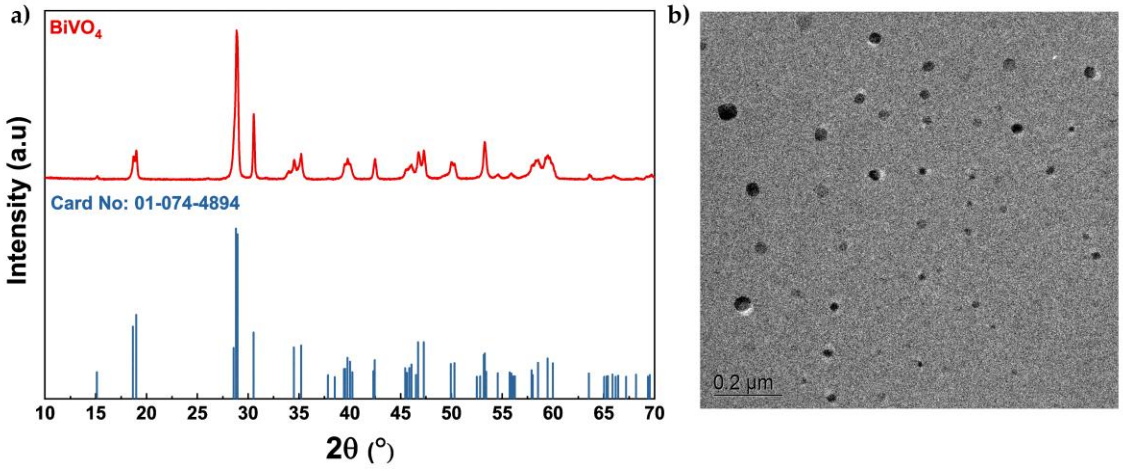

Figure 1. a) XRD pattern of the synthesized $BiVO_4$ sample together with vertical bars from card reference(No: 01-0074-4894); b) TEM image of $BiVO_4$ nanoparticles.

3.2. Textural, Vibrational, and Optical Properties of the Microwave-Synthesized $BiVO_4$

Furthermore, the textural features and vibrational modes of the synthesized $BiVO_4$ were characterized by nitrogen adsorption–desorption and FTIR spectroscopy (Figure 2). The N_2 adsorption–desorption isotherm (Figure 2a) is best described as Type II without a discernible hysteresis loop, typical of non-porous or macroporous solids. The BET surface area of the sample was calculated to be 7.5 m^2/g. The FTIR spectrum (Figure 2b) reveals several distinct absorption features between 500 and 800 cm^{-1}, which are characteristic of $BiVO_4$. A pronounced band centered at 603 cm^{-1} together with a shoulder at 805 cm^{-1} corresponds to the asymmetric and symmetric stretching vibrations of VO_4^{3-} units, while the band at 510 cm^{-1} is assigned to Bi–O stretching. In addition, a weak absorption at 1380 cm^{-1} is attributed to residual nitrate species originating from the precursors used during synthesis.

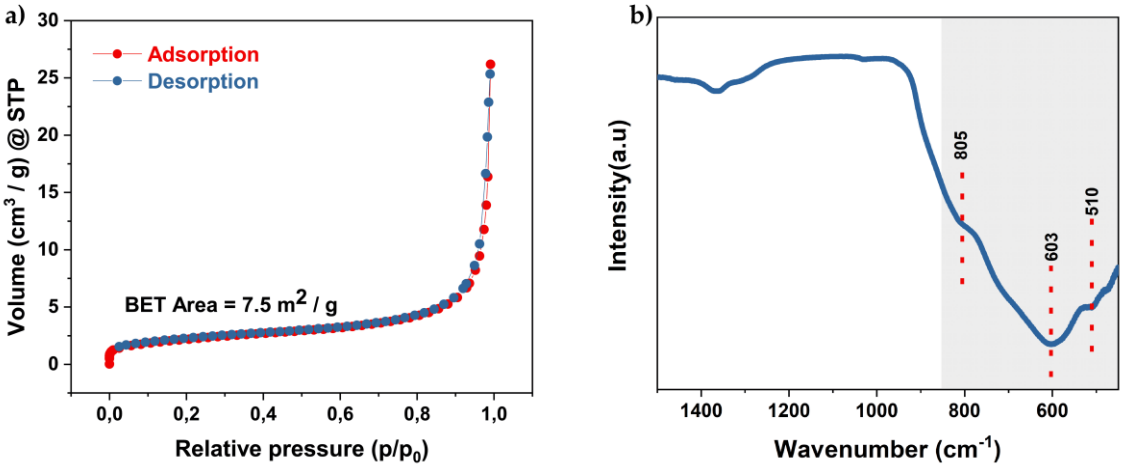

Figure 2. Textural and vibrational characterization of $BiVO_4$: a) N_2 adsorption–desorption isotherm; b) FTIR spectrum.

The optical band gap of the synthesized $BiVO_4$ was determined from the Tauc plot (using Eq. 2) and Eq. 3) assuming a direct allowed transition, yielding a value of 2.55 eV (Figure 3). This finding is in excellent agreement with previously reported values for monoclinic scheelite-type $BiVO_4$, which typically fall in the range of 2.4–2.6 eV [17]. The consistency of the obtained result with the literature further corroborates the formation of a pure monoclinic scheelite phase, as confirmed by XRD, and underlines the semiconductor's suitability for visible-light-driven photocatalytic applications. The

 doi:10.20944/preprints202510.0388.v1

band gap position ensures efficient utilization of the solar spectrum while maintaining sufficient oxidative potential, thus providing a favorable balance between light absorption and redox activity.

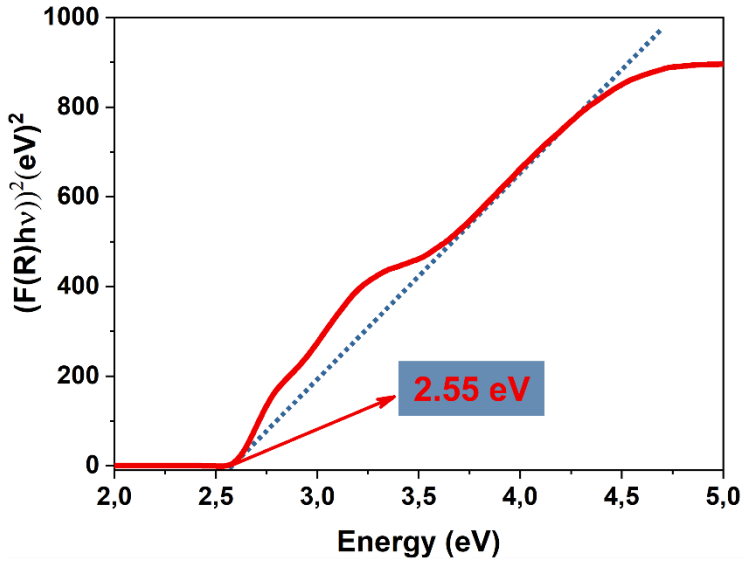

Figure 3. Tauc`s plot of $BiVO_4$ derived from Kubelka–Munk transformed UV–Vis diffuse reflectance data.

3.3. Photocatalytic Performance of the Microwave-Synthesized $BiVO_4$

AO7 in aqueous medium was used as a model pollutant to assess the visible-light photocatalytic activity of $BiVO_4$. Prior to irradiation, dye catalyst suspensions were stirred in the dark for 60 min to establish adsorption–desorption equilibrium. The influence of catalyst dosage and initial dye concentration on performance is evaluated below; pH was not systematically varied and remained near its native value (~4.5).

3.3.1. The Effect of Catalyst Dosage on the Degradation of Acid Orange 7

Figure 4 presents the time-resolved UV–Vis spectra of AO7 under visible-light irradiation in the presence of 15 mg $BiVO_4$. The principal visible band centered at λ_{max} = 484 nm decays steadily over 0–120 min, accompanied by a slight hypsochromic shift within the visible band, remaining centered at 484 nm. The shoulder within 440–520 nm progressively collapses, while the near-UV features around 250–320 nm attenuate more slowly, consistent with stepwise loss of conjugation in the dye chromophore [31].

 doi:10.20944/preprints202510.0388.v1

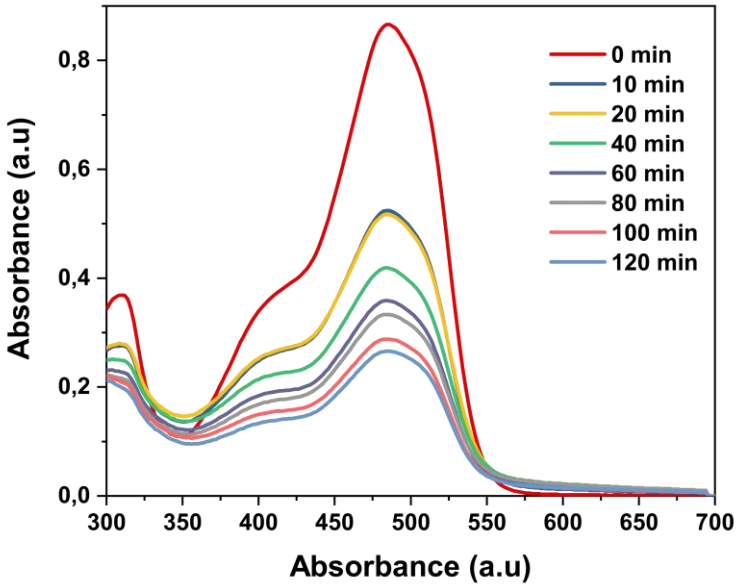

Figure 4. UV-Vis absorption spectra of the AO7 solution (20 ppm) for 15 mg of $BiVO_4$.

As shown in Figure 5, the influence of $BiVO_4$ dosage on the photocatalytic degradation of AO7 (20 ppm) under visible-light irradiation was investigated. Figure 5a illustrates the temporal decay of the normalized concentration (C/C_0) at the absorption maximum of AO7 (λmax ≈ 484 nm). In the absence of $BiVO_4$, only about 10% of AO7 was removed after 120 minutes, confirming that the degradation is primarily photocatalyst-driven. Increasing the catalyst dosage from 10 to 15 mg markedly enhanced degradation efficiency, with ~68% removal compared to ~55% for the lower loading. A further increase to 20 mg resulted in only a slight additional improvement, reaching ~72% after 120 minutes, indicating that the system operates close to its optimum catalyst loading.

The corresponding pseudo-first-order kinetic plots (Figure 5b) exhibit good linearity, consistent with the Langmuir–Hinshelwood model. The calculated rate constants increased with catalyst dosage, being lowest for 10 mg and highest for 20 mg, although the difference between 15 and 20 mg remained relatively small. This trend reflects a balance between the number of active surface sites and the efficiency of light utilization. At higher dosages, more reactive sites are available; however, excessive amounts can lead to light scattering, shielding effects, and partial particle aggregation, which ultimately limit further improvements in photocatalytic activity [32,33].

Based on these results, a dosage of 15 mg $BiVO_4$ was used for the investigation of the effect of the initial AO7 concentration, as it ensures nearly maximal efficiency while avoiding the drawbacks associated with higher loadings.

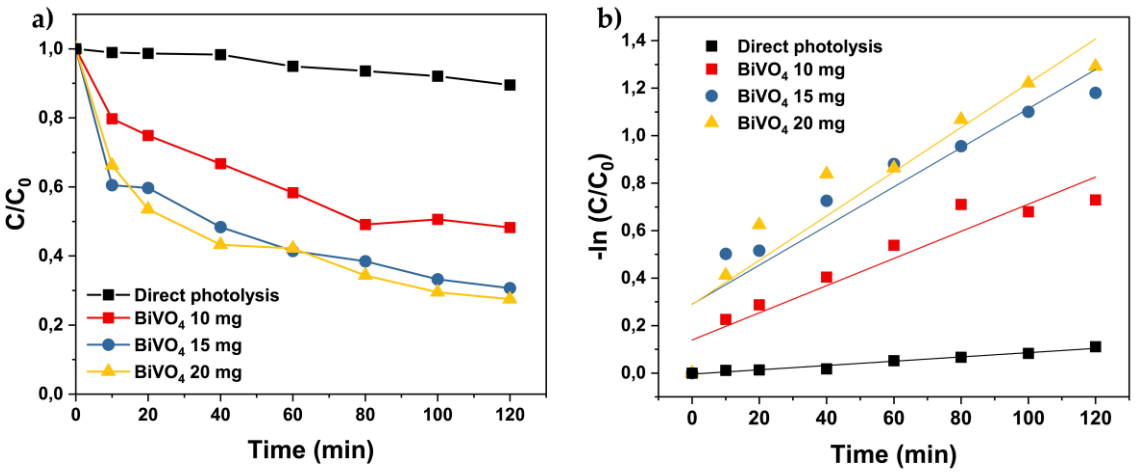

 doi:10.20944/preprints202510.0388.v1

Figure 5. Effect of $BiVO_4$ catalyst dosage on the photocatalytic degradation of AO7 (20 ppm) under visible light irradiation, including direct photolysis: a) temporal decay of normalized concentration (C/C_0) with time; b) pseudo-first-order kinetic plots.

3.3.2. Effect of the Initial Concentration of Pollutant Acid Orange 7 on Photocatalytic Degradation Efficiency

After establishing 15 mg $BiVO_4$ as the optimal catalyst dosage, the effect of the initial AO7 concentration was investigated. Figure 6a shows that the degradation efficiency decreases with increasing dye concentration. At 15 ppm, about 77% of AO7 was removed within 120 minutes, while the efficiency declined to ~69% at 20 ppm and ~70% at 25 ppm. This reduction is associated with stronger coloration of the solution at higher concentrations, which limits light penetration, as well as the saturation of active sites by excess dye molecules, reducing the availability of reactive oxygen species for photocatalytic reactions [34–36].

The kinetic plots (Figure 6b) confirm that the process follows pseudo-first-order kinetics, with linear fits yielding apparent rate constants of 0.0121 min^{-1} for 15 ppm, 0.0098 min^{-1} for 20 ppm, and 0.0100 min^{-1} for 25 ppm. The higher value obtained at 15 ppm indicates that the reaction proceeds faster at lower pollutant loads, while the decrease in k with increasing concentration reflects competition among dye molecules for both photons and active sites. Correlation coefficients ($R^2 > 0.95$) further support the applicability of the Langmuir–Hinshelwood kinetic model [37,38].

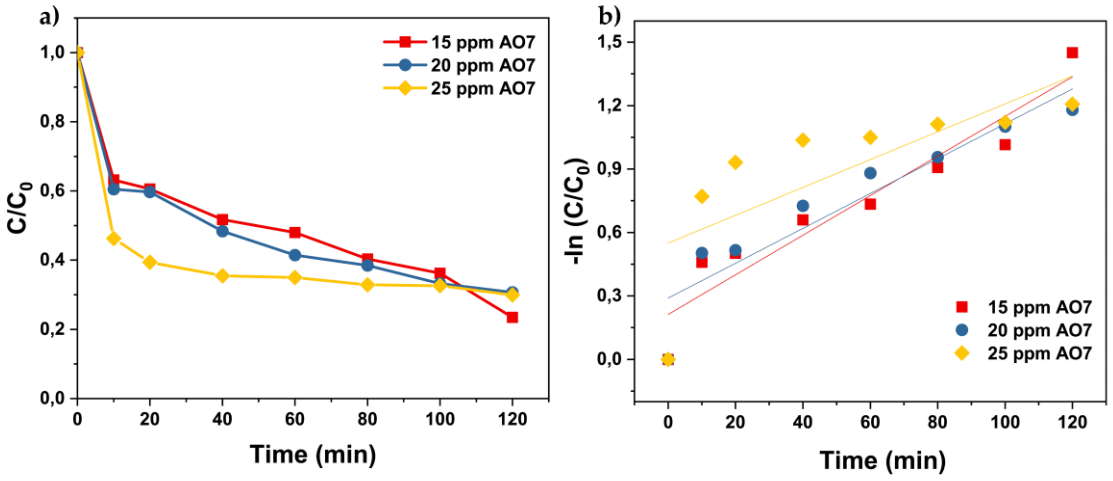

Figure 6. Effect of initial AO7 concentration (15 ppm, 20 ppm and 25 ppm) on the photocatalytic degradation over $BiVO_4$ (15 mg) under visible light irradiation: a) temporal decay of normalized concentration (C/C_0) with time; b) pseudo-first-order kinetic plots.

3.4. Possible Photocatalytic Pathway for the Degradation of Acid Orange 7

Based on the obtained photocatalytic results and supporting evidence from previously reported studies, the degradation pathway of AO7 under visible-light $HBiVO_4$ generates electron–hole pairs that initiate oxidative reactions mediated by ROS, mainly hydroxyl radicals (•OH) and superoxide anions ($•O_2^-$), in addition to direct hole oxidation (h^+). The degradation process starts with cleavage of the azo bond, giving rise to two main pathways. In the left pathway, sulfonated aromatic amines are formed and further oxidized to sulfonated hydroxybenzenes and benzoic acid–type derivatives. In the right pathway, hydroxylated naphthalene intermediates are produced, which undergo sequential transformations into hydroxylated naphthalenes, quinone derivatives, and benzoic acid–type compounds. Both branches subsequently converge toward low-molecular-weight aliphatic carboxylic acids, and the overall process ultimately leads to complete mineralization into CO_2 and H_2O.

 doi:10.20944/preprints202510.0388.v1

The stepwise degradation route illustrated in Figure 7 is consistent with the photocatalytic performance observed in this study and aligns with previously reported mechanisms of structurally similar azo dyes [39].

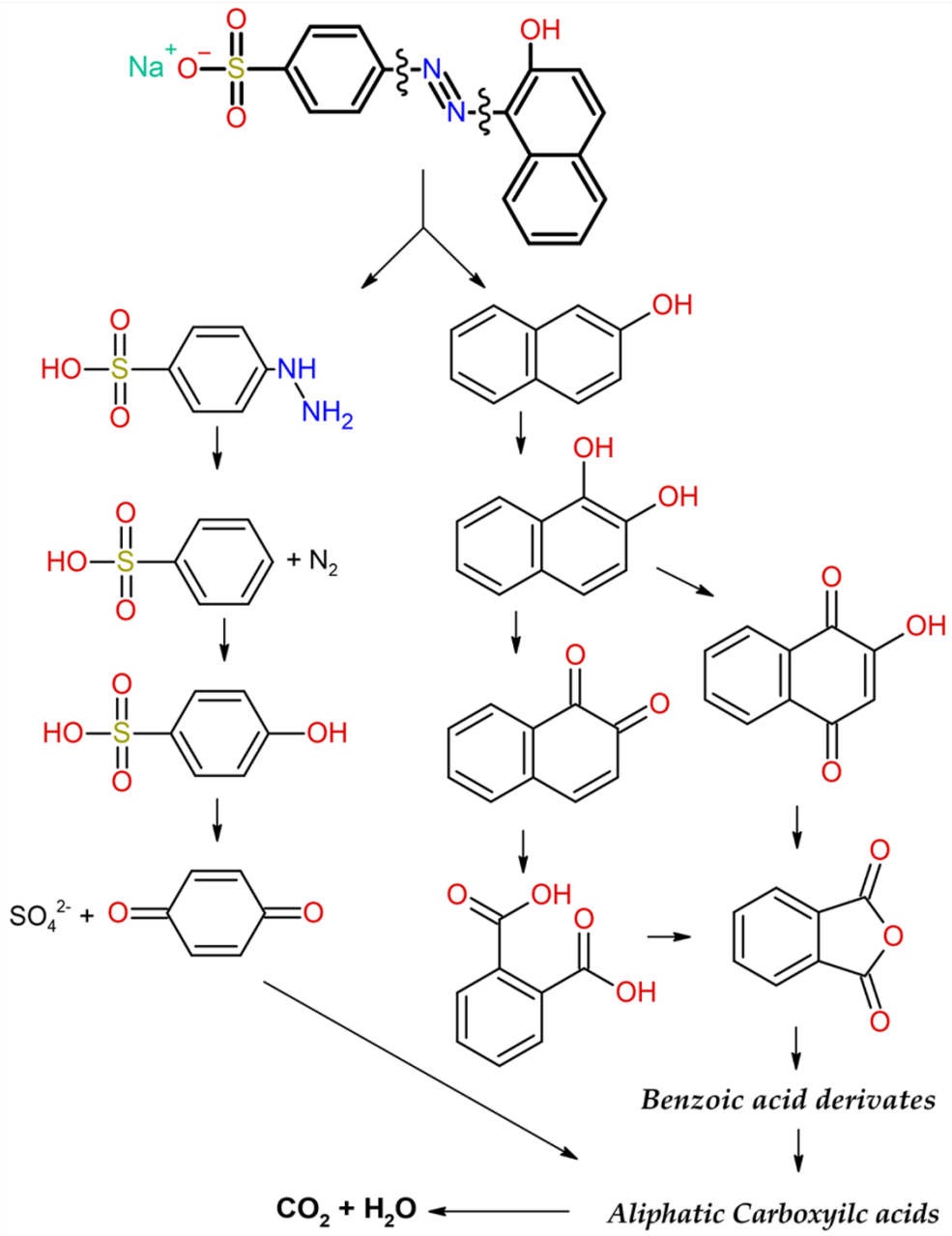

Figure 7. Proposed degradation pathway of AO7 under visible-light photocatalysis (Modified from [39]).

3.4. Antibacterial Properties

The results showed that $BiVO_4$ nanoparticles exhibited an antibacterial effect on *Escherichia coli* as a model indicator of pathogenic bacteria. After 4 hours of incubation with $BiVO_4$, the number of viable bacterial cells was significantly reduced compared to the control (Figure 8). On average, the inhibition of bacterial growth was 67.21 ± 3.15.

 doi:10.20944/preprints202510.0388.v1

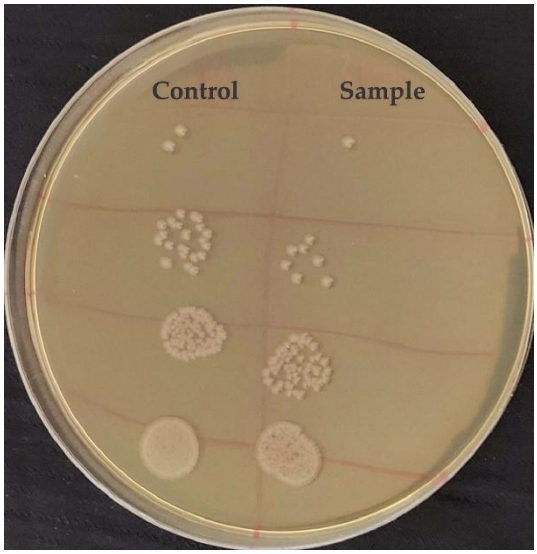

Figure 8. Photography of the TSA plate with serial dilutions of untreated *E. coli* (left) and the sample treated with UV-activated $BiVO_4$ nanoparticles (right).

Statistical analysis confirmed that this reduction was significant ($p < 0.05$), based on one-way ANOVA followed by Tukey's test. These findings indicate that $BiVO_4$ nanoparticles can effectively reduce the number of viable *E. coli* cells under the tested conditions.

The antibacterial effect of $BiVO_4$ nanoparticles against *Escherichia coli* can be attributed to a combination of multiple mechanisms. Due to their small crystalline size and high surface area-to-volume ratio, $BiVO_4$ nanoparticles can effectively penetrate the bacterial cell wall [26]. The positively charged metal ions on the nanoparticle surface interact electrostatically with the negatively charged bacterial cell wall components, leading to structural disruption and increased membrane permeability. This initial damage compromises the integrity of the bacterial cell and facilitates further nanoparticle entry. Furthermore, $BiVO_4$ could generate the formation of ROS, which induce oxidative stress in bacterial cells by damaging essential biomolecules such as lipids, proteins, and DNA. The oxidative damage results in inhibition of protein synthesis and interference with DNA replication processes, ultimately leading to bacterial cell death.

4. Conclusions

In this study, $BiVO_4$ nanoparticles were successfully synthesized by a rapid and eco-friendly microwave-assisted method. Structural and morphological analyses confirmed the formation of a pure monoclinic scheelite phase with nanoscale particle size and a specific surface area of 7.5 m^2/g. The optical band gap of 2.55 eV indicated visible-light responsiveness, making the material suitable for photocatalytic applications. Photocatalytic experiments demonstrated that the optimal catalyst dosage was 15 mg, which achieved nearly 80% degradation of AO7 (20 ppm) after 120 min under visible-light irradiation, while higher loadings provided only marginal improvement due to optical shielding and particle aggregation. Variation of the initial AO7 concentration further revealed that degradation efficiency and apparent rate constants decreased with increasing pollutant load, confirming the negative influence of excess dye molecules on photon penetration and active site availability. The reaction followed pseudo-first-order kinetics with R^2 values above 0.95, consistent with the Langmuir–Hinshelwood model. In addition, the $BiVO_4$ nanoparticles exhibited notable antibacterial activity, inhibiting the growth of *E. coli* by ~67%. Collectively, these findings demonstrate that microwave-synthesized $BiVO_4$ is a multifunctional material with strong potential for integrated wastewater remediation and disinfection under irradiation.

Author Contributions: Conceptualization, Dragana Marinković; investigation, Nataša Tot and Bojana Vasiljević; characterization, Anđela Pustak and Ivan Marić; antibacterial experiments, Slađana

 doi:10.20944/preprints202510.0388.v1

Davidović; data curation, Jovana Prekodravac Filipović; writing—original draft preparation, Nataša Tot and Bojana Vasiljević; writing—review and editing, Dragana Marinković; supervision, Dragana Marinković. All authors have read and agreed to the published version of the manuscript. All authors have read and agreed to the published version of the manuscript.

Funding: This research was funded by the Ministry of Science, Technological Development, and Innovation of the Republic of Serbia, grant number 451-03-136/2025-03/200017

Data Availability Statement: The raw data supporting the conclusions of this article will be made available by the authors on request

Acknowledgments: The authors are thankful to Dr. Yehezkel Yogev, Dr. Tanja Barudžija, and Prof. Dušan Mijin for providing TEM, XRD, and FTIR measurements.

Conflicts of Interest: The authors declare no conflicts of interest.

References

1. Moghimi Dehkordi, M.; Pournuroz Nodeh, Z.; Soleimani Dehkordi, K.; Salmanvandi, H.; Rasouli Khorjestan, R.; Ghaffarzadeh, M. Soil, Air, and Water Pollution from Mining and Industrial Activities: Sources of Pollution, Environmental Impacts, and Prevention and Control Methods. *Results Eng.* **2024**, *23*, 102729, doi:10.1016/j.rineng.2024.102729.
2. Shetty, S.S.; Deepthi, D.; Harshitha, S.; Sonkusare, S.; Naik, P.B.; Kumari, N.S.; Madhyastha, H. Environmental Pollutants and Their Effects on Human Health. *Heliyon* **2023**, *9*, e19496, doi:10.1016/j.heliyon.2023.e19496.
3. Tkaczyk, A.; Mitrowska, K.; Posyniak, A. Synthetic Organic Dyes as Contaminants of the Aquatic Environment and Their Implications for Ecosystems: A Review. *Sci. Total Environ.* **2020**, *717*, 137222, doi:10.1016/j.scitotenv.2020.137222.
4. Slama, H.B.; Chenari Bouket, A.; Pourhassan, Z.; Alenezi, F.N.; Silini, A.; Cherif-Silini, H.; Oszako, T.; Luptakova, L.; Golińska, P.; Belbahri, L. Diversity of Synthetic Dyes from Textile Industries, Discharge Impacts and Treatment Methods. *Appl. Sci.* **2021**, *11*, 6255, doi:10.3390/app11146255.
5. Benkhaya, S.; M'rabet, S.; El Harfi, A. Classifications, Properties, Recent Synthesis and Applications of Azo Dyes. *Heliyon* **2020**, *6*, e03271, doi:10.1016/j.heliyon.2020.e03271.
6. Kusumlata; Ambade, B.; Kumar, A.; Gautam, S. Sustainable Solutions: Reviewing the Future of Textile Dye Contaminant Removal with Emerging Biological Treatments. *Limnol. Rev.* **2024**, *24*, 126–149, doi:10.3390/limnolrev24020007.
7. Dutta, S.; Adhikary, S.; Bhattacharya, S.; Roy, D.; Chatterjee, S.; Chakraborty, A.; Banerjee, D.; Ganguly, A.; Nanda, S.; Rajak, P. Contamination of Textile Dyes in Aquatic Environment: Adverse Impacts on Aquatic Ecosystem and Human Health, and Its Management Using Bioremediation. *J. Environ. Manage.* **2024**, *353*, 120103, doi:10.1016/j.jenvman.2024.120103.
8. Daneshvar, N.; Aber, S.; Hosseinzadeh, F. Study of C.I. Acid Orange 7 Removal in Contaminated Water by Photo Oxidation Processes. *Glob. NEST J.* **2008**, *10*, 16–23, doi:10.30955/gnj.000435.
9. Kathi, S.; El Din Mahmoud, A. Trends in Effective Removal of Emerging Contaminants from Wastewater: A Comprehensive Review. *Desalination Water Treat.* **2024**, *317*, 100258, doi:10.1016/j.dwt.2024.100258.
10. Iervolino, G.; Vaiano, V.; Pepe, G.; Campiglia, P.; Palma, V. Degradation of Acid Orange 7 Azo Dye in Aqueous Solution by a Catalytic-Assisted, Non-Thermal Plasma Process. *Catalysts* **2020**, *10*, 888, doi:10.3390/catal10080888.
11. Tanos, F.; Razzouk, A.; Lesage, G.; Cretin, M.; Bechelany, M. A Comprehensive Review on Modification of Titanium Dioxide-Based Catalysts in Advanced Oxidation Processes for Water Treatment. *ChemSusChem* **2024**, *17*, e202301139, doi:10.1002/cssc.202301139.
12. Pham, H.-C.; Kim, K.-S. Effect of TiO_2 Thin Film Thickness on NO and SO_2 Removals by Dielectric Barrier Discharge-Photocatalyst Hybrid Process. *Ind. Eng. Chem. Res.* **2013**, *52*, 5296–5301, doi:10.1021/ie302713p.
13. Guo, Q.; Ma, Z.; Zhou, C.; Ren, Z.; Yang, X. Single Molecule Photocatalysis on TiO_2 Surfaces: Focus Review. *Chem. Rev.* **2019**, *119*, 11020–11041, doi:10.1021/acs.chemrev.9b00226.

 doi:10.20944/preprints202510.0388.v1

14. Etacheri, V.; Di Valentin, C.; Schneider, J.; Bahnemann, D.; Pillai, S.C. Visible-Light Activation of TiO_2 Photocatalysts: Advances in Theory and Experiments. *J. Photochem. Photobiol. C Photochem. Rev.* **2015**, *25*, 1–29, doi:10.1016/j.jphotochemrev.2015.08.003.
15. Kaiba, A.; Alansi, A.M.; Oubelkacem, A.; Chabri, I.; Hameed, S.T.; Afzal, N.; Rafique, M.; Qahtan, T.F. Sunlight-Driven Synthesis of TiO_2/$(MA)_2SnCl_4$ Nanocomposite Films for Enhanced Photocatalytic Degradation of Organic Pollutants. *Catalysts* **2025**, *15*, 214, doi:10.3390/catal15030214.
16. Ishigaki, T.; Nakada, Y.; Tarutani, N.; Uchikoshi, T.; Tsujimoto, Y.; Isobe, M.; Ogata, H.; Zhang, C.; Hao, D. Enhanced Visible-Light Photocatalytic Activity of Anatase-Rutile Mixed-Phase Nano-Size Powder Given by High-Temperature Heat Treatment. *R. Soc. Open Sci.* **2020**, *7*, 191539, doi:10.1098/rsos.191539.
17. Kamble, G.S.; Natarajan, T.S.; Patil, S.S.; Thomas, M.; Chougale, R.K.; Sanadi, P.D.; Siddharth, U.S.; Ling, Y.-C. BiVO4 As a Sustainable and Emerging Photocatalyst: Synthesis Methodologies, Engineering Properties, and Its Volatile Organic Compounds Degradation Efficiency. *Nanomaterials* **2023**, *13*, 1528, doi:10.3390/nano13091528.
18. Dolić, S.D.; Jovanović, D.J.; Štrbac, D.; Far, L.Đ.; Dramićanin, M.D. Improved Coloristic Properties and High NIR Reflectance of Environment-Friendly Yellow Pigments Based on Bismuth Vanadate. *Ceram. Int.* **2018**, *44*, 22731–22737, doi:10.1016/j.ceramint.2018.09.057.
19. Dolić, S.D.; Jovanović, D.J.; Smits, K.; Babić, B.; Marinović-Cincović, M.; Porobić, S.; Dramićanin, M.D. A Comparative Study of Photocatalytically Active Nanocrystalline Tetragonal Zyrcon-Type and Monoclinic Scheelite-Type Bismuth Vanadate. *Ceram. Int.* **2018**, *44*, 17953–17961, doi:10.1016/j.ceramint.2018.06.272.
20. Jeong, S.Y.; Choi, K.S.; Shin, H.-M.; Kim, T.L.; Song, J.; Yoon, S.; Jang, H.W.; Yoon, M.-H.; Jeon, C.; Lee, J.; Lee, J.; Lee, S. Enhanced Photocatalytic Performance Depending on Morphology of Bismuth Vanadate Thin Film Synthesized by Pulsed Laser Deposition. *ACS Appl. Mater. Interfaces* **2017**, *9*, 505–512, doi:10.1021/acsami.6b15034.
21. Jelić, S.T.; Ćirković, J.; Jovanović, J.; Novaković, T.; Podlogar, M.; Mitrić, J.; Branković, G.; Branković, Z. High Efficiency Solar Light Photocatalytic Degradation of Mordant Blue 9 by Monoclinic $BiVO_4$ Nanopowder. *Mater. Chem. Phys.* **2025**, *333*, 130341, doi:10.1016/j.matchemphys.2024.130341.
22. Regmi, C.; Dhakal, D.; Lee, S.W. Visible-Light-Induced Ag/$BiVO_4$ Semiconductor with Enhanced Photocatalytic and Antibacterial Performance. *Nanotechnology* **2018**, *29*, 064001, doi:10.1088/1361-6528/aaa052.
23. Zhang, A.; Zhang, J. Effects of Europium Doping on the Photocatalytic Behavior of BiVO4. *J. Hazard. Mater.* **2010**, *173*, 265–272, doi:10.1016/j.jhazmat.2009.08.079.
24. Drisya, K.T.; Solís-López, M.; Ríos-Ramírez, J.J.; Durán-Álvarez, J.C.; Rousseau, A.; Velumani, S.; Asomoza, R.; Kassiba, A.; Jantrania, A.; Castaneda, H. Electronic and Optical Competence of TiO_2/$BiVO_4$ Nanocomposites in the Photocatalytic Processes. *Sci. Rep.* **2020**, *10*, 13507, doi:10.1038/s41598-020-69032-9.
25. Ran, J.-H.; Fei, X.; Ni, L.; Telegin, F. Enhanced Photocatalytic Degradation of Acid Orange 7 by AgBr/$BiVO_4$ under Visible Light. *J. Fiber Bioeng. Inform.* **2018**, *11*, 151–161, doi:10.3993/jfbim00283.
26. Bulut, D.T. Exploring the Dual Role of BiVO4 Nanoparticles: Unveiling Enhanced Antimicrobial Efficacy and Photocatalytic Performance. *J. Sol-Gel Sci. Technol.* **2025**, *114*, 198–222, doi:10.1007/s10971-025-06682-z.
27. Pramila, S.; Nagaraju, G.; Mallikarjunaswamy, C.; Latha, K.C.; Chandan, S.; Ramu, R.; Rashmi, V.; Lakshmi Ranganatha, V. Green Synthesis of BiVO4 Nanoparticles by Microwave Method Using *Aegle marmelos* Juice as a Fuel: Photocatalytic and Antimicrobial Study. *Anal. Chem. Lett.* **2020**, *10*, 298–306, doi:10.1080/22297928.2020.1785935.
28. Marinković, D.; Righini, G.C.; Ferrari, M. Advances in Synthesis and Applications of Bismuth Vanadate-Based Structures. *Inorganics* **2025**, *13*, 268, doi:10.3390/inorganics13080268.
29. Marinković, D.; Righini, G.C.; Ferrari, M. Synthesis, Optical, and Photocatalytic Properties of the $BiVO_4$ Semiconductor Nanoparticles with Tetragonal Zircon-Type Structure. *Photonics* **2025**, *12*, 438, doi:10.3390/photonics12050438.
30. Li, B.; Gao, X.; Qu, J.; Xiong, F.; Xuan, H.; Jin, Y.; Yuan, H. Visible-Light-Driven Antimicrobial Activity and Mechanism of Polydopamine-Reduced Graphene Oxide/BiVO4 Composite. *Int. J. Mol. Sci.* **2022**, *23*, 7712, doi:10.3390/ijms23147712.

 doi:10.20944/preprints202510.0388.v1

31. Zhang, S.-J.; Yu, H.-Q.; Li, Q.-R. Radiolytic Degradation of Acid Orange 7: A Mechanistic Study. *Chemosphere* **2005**, *61*, 1003–1011, doi:10.1016/j.chemosphere.2005.03.008.
32. Iqbal, N.; Huang, X.; Mohamedali Hamid, K.; Yuan, H.; Batool, I.; Yang, Y. Efficient Visible-Light-Driven Photocatalysis of $BiVO_4$@Diatomite for Degradation of Methoxychlor. *Catalysts* **2025**, *15*, 672, doi:10.3390/catal15070672.
33. Maran, M.A.; Zheng, A.L.T.; Tan, H.Y.; Sarbini, S.R.; Tan, K.B.; Boonyuen, S.; Wong, K.K.S.; Chung, E.L.T.; Lease, J.; Andou, Y. Assessing the Photocatalytic Performance of Hydrothermally Synthesized Fe-Doped BiVO4 Under Low-Intensity UV Irradiation. *Arab. J. Sci. Eng.* **2025**, doi:10.1007/s13369-025-10278-8.
34. Nunes, M.J.; Lopes, A.; Pacheco, M.J.; Ciríaco, L. Visible-Light-Driven AO7 Photocatalytic Degradation and Toxicity Removal at Bi-Doped $SrTiO_3$. *Materials* **2022**, *15*, 2465, doi:10.3390/ma15072465.
35. Reza, K.M.; Kurny, A.; Gulshan, F. Parameters Affecting the Photocatalytic Degradation of Dyes Using TiO_2: A Review. *Appl. Water Sci.* **2017**, *7*, 1569–1578, doi:10.1007/s13201-015-0367-y.
36. Khan, S.; Noor, T.; Iqbal, N.; Yaqoob, L. Photocatalytic Dye Degradation from Textile Wastewater: A Review. *ACS Omega* **2024**, *9*, 21751–21767, doi:10.1021/acsomega.4c00887.
37. Asenjo, N.G.; Santamaría, R.; Blanco, C.; Granda, M.; Álvarez, P.; Menéndez, R. Correct Use of the Langmuir–Hinshelwood Equation for Proving the Absence of a Synergy Effect in the Photocatalytic Degradation of Phenol on a Suspended Mixture of Titania and Activated Carbon. *Carbon* **2013**, *55*, 62–69, doi:10.1016/j.carbon.2012.12.010.
38. Phanichphant, S.; Nakaruk, A.; Chansaenpak, K.; Channei, D. Evaluating the Photocatalytic Efficiency of the $BiVO_4$/rGO Photocatalyst. *Sci. Rep.* **2019**, *9*, 16091, doi:10.1038/s41598-019-52589-5.
39. Viswanathan, B. Photocatalytic Degradation of Dyes: An Overview. *Curr. Catal.* **2018**, *7*, 99–121, doi:10.2174/2211544707666171219161846.